





Cite this: DOI: 10.1039/d5ey00169b

Strategic synergism in CO₂ and biomass valorization into sustainable solar fuels *via* stable hybrid halide perovskites: unlocking untapped potential

Bhawna Rawat,^a Ankita Kumari,^b Manvi Sachdeva,^a Himanshu Bhatt,^a Dibyajyoti Ghosh,^b Hirendra N. Ghosh,^{*c} Rajenahally V. Jagadeesh ^{*de} and Kamalakannan Kailasam ^{*a}

Sunlight-driven integration of photocatalytic CO₂ reduction with biomass feedstock valorization constitutes a highly efficient strategy for the synergistic production of multi-electron products and high-value fine chemicals, adhering to photo-chemical circular economy and sustainability. To date, no halide perovskite has been utilized for CO₂ reduction coupled with biomass oxidation as the development of more stable, efficient, reusable, and non-toxic halide perovskites continues to be challenging. Herein, we report the room-temperature synthesis of methylammonium tin bromide (MA₂SnBr₆) quantum dots (QDs), a vacancy-ordered hybrid halide perovskite (HHP), without additional capping agents. These novel QDs maintain structural integrity in air, moisture, and polar solvents, addressing a significant issue associated with halide perovskites. Remarkably, the MA₂SnBr₆ QDs remain stable under ambient conditions even after 1 year, as confirmed by PXRD analysis. Interestingly, MA₂SnBr₆ achieved exceptionally high electron consumption rates (R_e) of 5110 $\mu\text{mol g}^{-1} \text{h}^{-1}$ and 12 383 $\mu\text{mol g}^{-1} \text{h}^{-1}$ for CO₂ reduction under simulated and natural sunlight, respectively, outperforming previous systems. *In situ* transient studies demonstrate that the photogenerated electrons of MA₂SnBr₆ diffuse from the conduction band to trap states, reducing CO₂, while synergistically photogenerated holes oxidize biomass-derived alcohols. Additionally, *in situ* EPR experiments were performed to unravel mechanistic insights. Computational studies identify the Br p-orbitals of MA₂SnBr₆ as the reaction centre for CO₂ reduction. Consequently, this work introduces a lead-free, single-component material that operates without a co-catalyst, sacrificial agent or redox additive, offering a promising path towards achieving photoredox processes in a more sustainable and efficient manner.

Received 12th June 2025,
Accepted 29th August 2025

DOI: 10.1039/d5ey00169b

rsc.li/eescatalysis

Broader context

The most challenging aspect and bottleneck in photocatalysis is the effective employment of charge carriers in the most sustainable manner for synergistic reduction and oxidation processes while achieving a robust catalyst without the use of co-catalysts, sacrificial agents, or redox additives. Particularly, in tackling excessive CO₂ emissions, solar energy provides a sustainable route to transform CO₂ into fuels, achieving carbon neutrality. Photocatalytic CO₂ reduction in synergism with biomass valorization under sunlight offers a highly effective approach towards “Photo-biorefinery.” This study also breaks the perception of the instability of halide perovskites for photocatalytic organic transformation and photoredox reactions. Halide perovskites are widely explored for CO₂-to-CO conversion; however, deep-reduced fuels, such as CH₄, still face a challenge with perovskites. This study not only presents the facile mechanochemical synthesis of novel lead-free hybrid halide perovskites in MA₂SnBr₆ QDs, but also addresses the limitation of conventional halide perovskites—particularly their instability, toxicity, low efficiency, and poor reusability. Eventually, the single-component perovskite achieved record-high production of CO and CH₄ under natural sunlight, even without any co-catalyst or sacrificial agent—outperforming the existing halide perovskite photocatalysts. These findings uniquely couple the production of fine chemicals, such as vanillin, veratraldehyde, and 2-phenoxy-1-phenylethanone, with the generation of solar CO and CH₄ fuels, thus achieving a “photo-chemical circular economy.”

^a Institute of Nano Science and Technology (INST), Knowledge City, Sector 81, SAS Nagar, Manauli PO, 140306 Mohali, Punjab, India. E-mail: kamal@inst.ac.in

^b Department of Chemistry, Indian Institute of Technology, Delhi, Hauz Khas, New Delhi 110016, India

^c School of Chemical Sciences, National Institute of Science and Education Research (NISER), Bhubaneswar, Odisha 752050, India

^d Leibniz-Institut für Katalyse, Albert-Einstein-Straße 29a, 18059 Rostock, Germany

^e Nanotechnology Centre, Centre for Energy and Environmental Technologies, VŠB–Technical University of Ostrava, Ostrava-Poruba, Czech Republic



Introduction

Nature, in all its ingenuity, achieves extraordinary feats such as photosynthesis, an effortlessly executed complex process. However, the real challenge is in replicating these natural phenomena, a task that persistently advances the boundaries of scientific innovations. Mimicking natural photosynthesis, through the coupling of CO₂ reduction with H₂O oxidation to achieve carbon neutrality, represents an ideal green process in the development of artificial photosynthesis.¹ CO₂ itself plays a vital role in maintaining the ecological balance of the Earth. However, the increased use of non-renewable fossil-based feedstocks and rapid industrialization are leading to an increase in CO₂ levels, which represents a bottleneck in sequestering CO₂ in fuels to reduce our carbon footprints.² The CO₂ conversion to CO and CH₄ has gained significant scientific attention³ with the assistance of various photocatalysts such as metal oxides, metal chalcogenides, metal complexes, organic semiconductors, and perovskites. However, the H₂O oxidation follows slow kinetics that can be replaced by biomass oxidation to effectively utilize the photogenerated holes to drive the desired oxidation reaction. Integrating photocatalytic CO₂ reduction with biomass valorization using sunlight presents a highly efficient strategy for the synergistic production of solar fuels and value-added fine chemicals that meet the criteria of chemical economy and sustainability.⁴ In this regard, to date, no halide perovskite has been employed for synergistic CO₂ reduction with biomass valorization.

Halide perovskites have emerged as promising advanced materials,⁵ which find increasing applications in catalysis.⁶ Their remarkable properties such as high absorption coefficient, exceptional charge carrier mobility, long diffusion length, highly crystalline structure and low binding energy of excitons, as well as tuning of band gap by changing the halide, established them as highly essential materials, opening new opportunities in catalysis.⁷ Despite significant achievements in halide perovskite-based materials, still advancements have to be made to maintain their stability and non-toxicity, thereby enhancing their broad applicability.^{7,8} To achieve this, a major focus is on replacing the A cation in the ABX₃ structure of perovskites. The scientific focus was also shifted majorly towards the replacement of the B cation,⁹ which stands for Pb in many of the previously reported works as Pb-based perovskites are toxic for our precious nature. Therefore, the development of lead-free halide perovskites without compromising their properties and efficiency is of prime importance. In this regard, we turned our interest to focus on the preparation of lead-free perovskite materials and their applications.

In our current work, we aimed to address four major challenges of the perovskite's domain, namely stability, reusability, toxicity, and efficiency of hybrid halide perovskites (HHPs).¹⁰ To tackle these issues, we synthesized a vacancy-ordered HHP, specifically MA₂SnBr₆ QDs, which had not been explicitly synthesized so far. MA₂SnBr₆ was synthesized *via* a greener approach, a simple yet effective solvent-free mechanochemical synthesis at room temperature without the use of additional capping agents. Interestingly, the synthesized

MA₂SnBr₆ QDs maintained structural integrity in air and moisture, addressing a common issue with HHPs. To our surprise, these QDs are also stable in polar solvents such as isopropanol, ethanol, and acetonitrile, overcoming a major challenge typically encountered with halide perovskites. Remarkably, the significance of QDs is now widely recognized, as emphasized by the 2023 Nobel Prize in Chemistry awarded for the discovery and synthesis of QDs, highlighting their wide-ranging applications. Inspired by this notable achievement, the potential use of the synthesized air and moisture-resistant MA₂SnBr₆ QDs has been investigated for the photocatalytic conversion of renewable resources, including carbon dioxide and biomass-derived compounds, under sunlight, mimicking the process of artificial photosynthesis.

Therefore, for performing artificial photosynthesis, MA₂SnBr₆ QDs were applied for the simultaneous photocatalytic reduction of CO₂ into CO and CH₄ and oxidation of biomass-based alcohols and lignin model compounds to carbonyl compounds under natural sunlight. In this context, halide perovskites have been considerably explored for photocatalytic CO₂ reduction;¹¹ however, the majority of these relied on Pb-based perovskites,^{12–36} which are not compatible with the sustainability goals of carbon capture, utilization, and fixation.¹¹ Further, previous studies employed co-catalyst-loaded perovskites,^{12,13,19,29} ternary systems,^{23,25,32,37} and complex heterojunctions^{37–43} to increase the photocatalytic activity, yet not succeeded in a promising manner. Moreover, the complex synthesis procedure of these photocatalytic systems makes them economically non-viable, thereby limiting their potential for large-scale process. Additionally, the full potential of halide perovskites has not been realized because they were not employed for the simultaneous photo-reduction of CO₂ and photo-oxidation of biomass-based feedstocks. Thus, during the photo-reduction of CO₂, the unutilized photogenerated holes are employed for oxidation reactions. In response, MA₂SnBr₆ QDs serves as Pb-free, single-component systems offering a synergistic way for utilizing photogenerated electrons for CO₂ reduction to CO and CH₄, while performing the conversion of biomass-derived compounds using photogenerated holes. Thus a sustainable pathway has been adapted without loading any co-catalyst and even without any sacrificial agent.

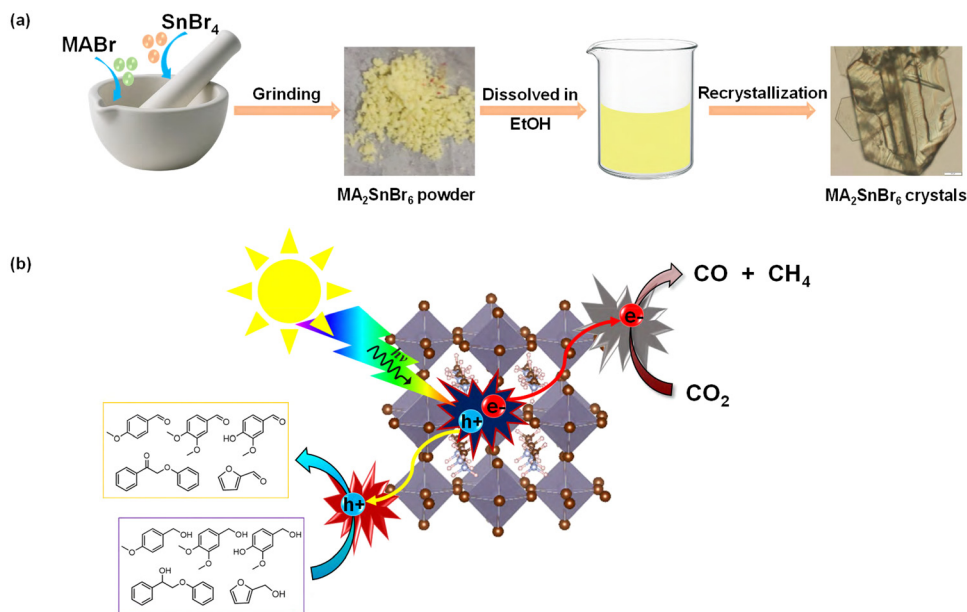
Results and discussion

Synthesis and characterization of MA₂SnBr₆ QDs

The MA₂SnBr₆ QDs were synthesized for the first time *via* a simple mechanochemical route and employed for photocatalytic CO₂ reduction in synergism with the oxidation of biomass-derived compounds (Scheme 1a and b). The initial characterization was conducted by powder X-ray diffraction (PXRD) of the samples, as shown in Fig. S1. The PXRD pattern of MA₂SnBr₆ showed no peak corresponding to the reactants, MABr or SnBr₄, confirming the successful synthesis of pure MA₂SnBr₆ perovskites.⁴⁴

The MA₂SnBr₆ QDs were kept under ambient conditions and PXRD was conducted after one year, where no change was observed in the PXRD pattern of MA₂SnBr₆, demonstrating the retention of the MA₂SnBr₆ crystalline structure even after





Scheme 1 Schematic of (a) the synthesis route followed for MA_2SnBr_6 QDs, and (b) MA_2SnBr_6 perovskite QDs applied for photocatalytic CO_2 reduction coupled with oxidation of biomass-derived compounds.

one year (Fig. 1a). The diffuse reflectance UV-vis (DR UV-vis) spectrum of MA_2SnBr_6 is presented in Fig. 1b, revealing an absorbance onset at 462 nm, and the corresponding Tauc plot indicates a band gap of 2.80 eV (Fig. 1c). To investigate the surface characteristics, initially, a survey scan of MA_2SnBr_6 was recorded by X-ray photoelectron spectroscopy (XPS). The survey scan showed the presence of C, N, Sn, and Br elements in the perovskite sample with elemental atomic compositions of 25.9%, 13.7%, 11.4%, and 49.0%, respectively (Fig. S2a), confirming the

Br-enriched surface in the synthesized MA_2SnBr_6 material. The high-resolution XPS (HR-XPS) of Sn 3d was recorded, which showed two peaks at binding energies of 487.3 and 495.8 eV corresponding to Sn 3d_{5/2} and Sn 3d_{3/2}, respectively (Fig. 1d). These peaks confirmed the presence of Sn in the +4 oxidation state. The HR-XPS of Br 3d was deconvoluted into two peaks centered at 69.0 eV and 70.2 eV attributed to binding energies of Br 3d_{5/2} and Br 3d_{3/2}, respectively (Fig. S2b). Further, the HR-XPS of C 1s was deconvoluted into two peaks centered at 284.7 eV and

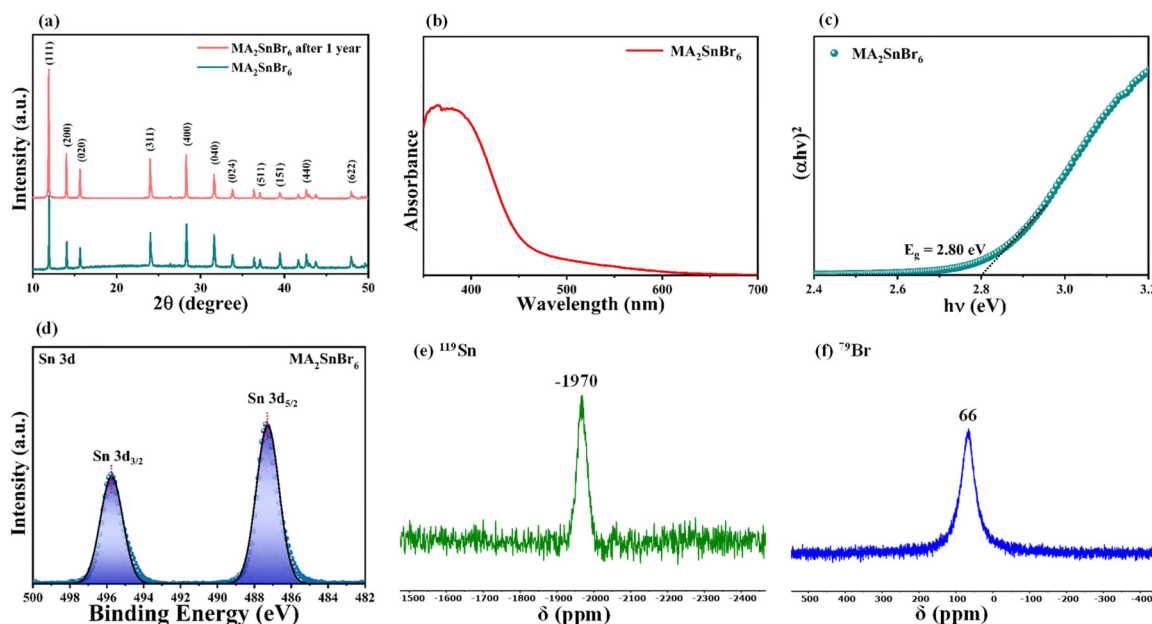


Fig. 1 (a) PXRD patterns of MA_2SnBr_6 after one year; (b) powder DR UV-Vis spectra of MA_2SnBr_6 ; (c) Tauc plot of MA_2SnBr_6 ; (d) Sn 3d HR-XPS of MA_2SnBr_6 ; and MAS solid-state NMR spectra of (e) ^{119}Sn , and (f) ^{79}Br of MA_2SnBr_6 .



286.2 eV corresponding to the C–C/C–H and C–N binding energies, indicating the presence of methyl and methyl ammonium groups, respectively, in MA_2SnBr_6 (Fig. S2c). The C–N peak also appeared in the N 1s HR-XPS at 402.0 eV, further confirming the presence of methyl ammonium groups (Fig. S2d).

The chemical structure of MA_2SnBr_6 was also scrutinized by CP/MAS solid-state NMR spectroscopy, where the ^{119}Sn NMR spectra showed a peak with a chemical shift at -1970 ppm (Fig. 1e), indicating the presence of single sites of the Sn atom. Then, ^{79}Br NMR was also recorded to see the bromine environment in MA_2SnBr_6 . Notably, a single peak was observed at 66 ppm (Fig. 1f), stipulating the presence of one type of Br atoms, which are bonded to Sn in the perovskite structure. Next, the ^{13}C NMR spectra showed a peak at a chemical shift of 33.2 ppm (Fig. S3a) which corresponded to the $-\text{CH}_3$ group present in the MA_2SnBr_6 perovskite. In the ^{15}N NMR spectra, the peak observed at 31.7 ppm (Fig. S3b) was attributed to the ammonium group present in MA_2SnBr_6 . Subsequently, the chemical structure of MA_2SnBr_6 was characterized by ATR-FTIR spectroscopy (Fig. S4), where the stretching frequency at 900 cm^{-1} was attributed to the rocking vibration of CH_3NH_3^+ , the stretching at 1473 cm^{-1} corresponded to C–H bending, the peak at 1574 cm^{-1} was assigned to the N–H bending vibration, the peak at 3180 cm^{-1} was assigned to the N–H asymmetric stretching vibration, and the peak at 543 cm^{-1} was assigned to the Sn–Br stretching vibration. The Raman spectral analysis was performed to study the vibrational properties of MA_2SnBr_6 , where the Br–Sn–Br asymmetric bending deformation was observed at $\delta(\text{F}_{2g}) = 119.5\text{ cm}^{-1}$, Sn–Br asymmetric stretching was observed at $\nu(\text{E}_g) = 140.7\text{ cm}^{-1}$ and Sn–Br symmetric stretching was noticed at 185.8 cm^{-1} (Fig. S5).

In the microscopy study, the FESEM images were acquired to examine the morphology of MA_2SnBr_6 , revealing a particle-like

structure (Fig. 2a). To gain a clear insight, transmission electron microscopy (TEM) was performed, unveiling clusters of small particles for the MA_2SnBr_6 perovskite (Fig. 2b). The high-resolution TEM (HR-TEM) image provided a detailed picture, where it was found that the MA_2SnBr_6 perovskites were actually QDs. Further analysis of HR-TEM provided d-spacing values of 0.36 nm and 0.28 nm corresponding to the (311) and (040) planes, respectively (Fig. 2d). Additionally, the TEM analysis showed that these QDs have a size range of 3–4.6 nm with an average particle size of 3.8 ± 0.3 nm (Fig. 2f), and the inset of Fig. 2f presents the particle size distribution of MA_2SnBr_6 QDs. To assess the long-term stability of MA_2SnBr_6 , TEM and HRTEM images of the same sample stored under ambient conditions for one year were recorded (Fig. 2c and 2e), and its morphology and dispersity with as-synthesized MA_2SnBr_6 were compared. The TEM image of MA_2SnBr_6 (after one year) shows clusters of small particles (Fig. 2c), and the HR-TEM images reveal agglomerated QDs for MA_2SnBr_6 (Fig. 2e) with an average particle size of 3.7 ± 0.3 nm comparable to that of the freshly synthesized material. Additionally, the measured lattice fringes exhibited a d-spacing value of 0.36 nm corresponding to the (311) plane and 0.28 nm representing the (040) plane (Fig. 2e). Hence, the morphology, dispersity, and crystallinity of MA_2SnBr_6 remained well-preserved even after one year of exposure to air and moisture. The observations, supported by PXRD, TEM, and HRTEM analyses, collectively demonstrated the excellent long-term stability of the MA_2SnBr_6 perovskite.

Further, the thermogravimetric analysis (TGA) indicates that MA_2SnBr_6 exhibits good thermal stability up to 230°C , after which decomposition begins, attributed to the degradation of the methylammonium group in MA_2SnBr_6 (Fig. S6a). Next, MA_2SnBr_6 was dissolved in different polar solvents such as ethanol, isopropanol, acetonitrile, and ethyl acetate, and the

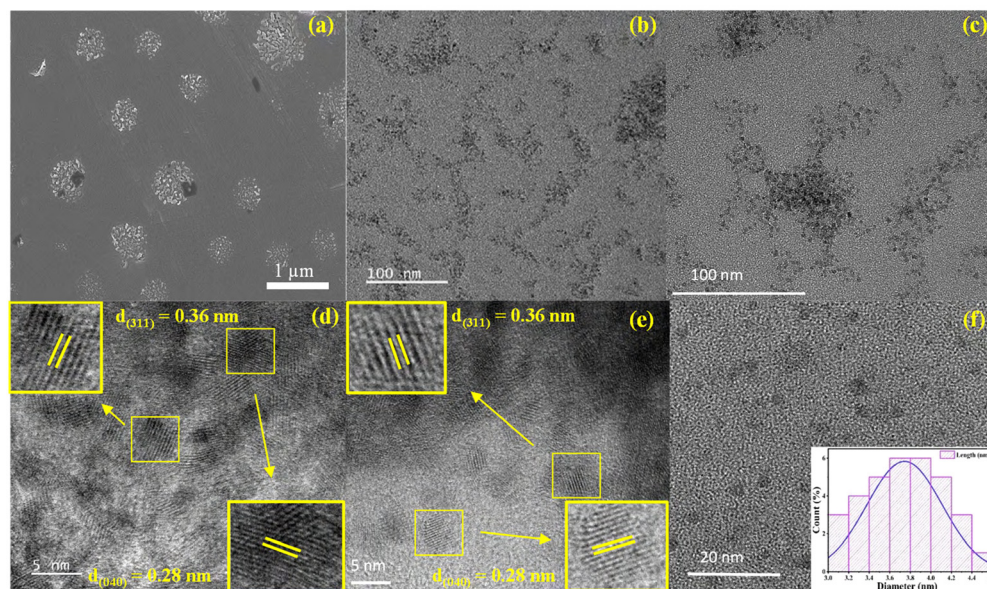


Fig. 2 (a) FESEM image; TEM image of (b) fresh MA_2SnBr_6 and (c) MA_2SnBr_6 after one year; HR-TEM image of (d) fresh MA_2SnBr_6 and (e) MA_2SnBr_6 after one year; and (f) TEM image showing the distribution of MA_2SnBr_6 QDs (inset shows the particle size distribution of QDs).



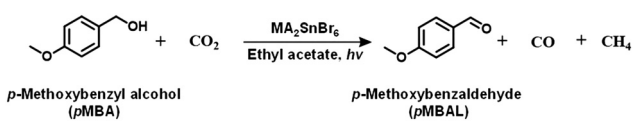
collected samples were subjected to PXRD analysis (Fig. S6b). No changes were observed in the PXRD patterns, demonstrating the excellent chemical resilience of the MA_2SnBr_6 perovskite in polar solvents. Further, the electronic band structure of MA_2SnBr_6 was deduced from ultraviolet photoelectron spectroscopy (UPS) measurements (Fig. S6c), and the corresponding schematic of the band energy diagram is presented in Fig. S6d.

Photocatalytic performance of MA_2SnBr_6 QDs

Showcasing their sufficient reduction potential, the MA_2SnBr_6 QDs were employed for photocatalytic CO_2 reduction coupled with the simultaneous oxidation of biomass-derived alcohols and lignin model compounds under simulated light (Oriel AM 1.5 with 100 mW cm^{-2} intensity). The electrons from the MA_2SnBr_6 photocatalyst were utilized to carry out CO_2 photoreduction producing CO and CH_4 as reduced products, while the holes are synergistically employed for the selective oxidation of *p*-methoxybenzyl alcohol (pMBA) to *p*-methoxybenzaldehyde (pMBAL) as the model compound. The corresponding gas chromatography-mass spectrometry (GC-MS) chromatogram is presented in Fig. S7. Notably, the single-system MA_2SnBr_6 QDs achieved impressive production rates (Table 1) of $483 \mu\text{mol g}^{-1} \text{ h}^{-1}$ for CO and $518 \mu\text{mol g}^{-1} \text{ h}^{-1}$ for

CH_4 , alongside a yield of $253 \mu\text{mol g}^{-1} \text{ h}^{-1}$ of pMBAL with $>99\%$ of selectivity over 24 h (entry 1, Fig. 3a). In contrast, the optimized reaction performed without the catalyst resulted in no production of CO, CH_4 , or pMBAL. Similarly, when the reaction was conducted in the absence of light, only a yield of $13 \mu\text{mol g}^{-1} \text{ h}^{-1}$ of pMBAL was observed, with no formation of CO and CH_4 (Fig. 3a). These results highlighted the necessity of both the catalyst and light for the effective reduction of CO_2 and oxidation of pMBA. To evaluate the practical applicability of MA_2SnBr_6 QDs for CO_2 reduction with simultaneous pMBA oxidation, the photocatalytic reaction was carried out under natural sunlight. The reaction setup under sunlight is depicted in Fig. S8a, and the corresponding sunlight intensity and temperature are plotted in Fig. S8b. Under natural sunlight, the reaction offered impressive yields $1218.9 \mu\text{mol g}^{-1} \text{ h}^{-1}$ of CO and $1243.2 \mu\text{mol g}^{-1} \text{ h}^{-1}$ of CH_4 with a yield of $167 \mu\text{mol g}^{-1} \text{ h}^{-1}$ of pMBAL within 6 h. Further optimization extended the reaction time to 48 h during which a continuous increase in the yields of CO, CH_4 , and pMBAL was observed (Fig. 3b). Subsequently, the apparent quantum yield (AQY%) was measured under different monochromatic light irradiation. The AQY% was determined based on CH_4 production under irradiation of monochromatic

Table 1 Photocatalytic CO_2 reduction in synergism with biomass-derived alcohol oxidation^a

						
Entry	Substrate	Product	Oxidation product		Reduction product	
			Conversion ($\mu\text{mol g}^{-1} \text{ h}^{-1}$)	Selectivity (%)	CO ($\mu\text{mol g}^{-1} \text{ h}^{-1}$)	CH_4 ($\mu\text{mol g}^{-1} \text{ h}^{-1}$)
(1)			253	> 99	483	518
(2)			354	> 99	779	48
(3)			63	> 99	340	64
(4)			416	> 99	597	66
(5)			34	> 99	539	0
(6)			117	> 99	119	238
(7)			225	> 99	562	303
(8)			250	> 99	275	485

^a Reaction conditions: 5 mg photocatalyst, 5 mL ethyl acetate, 0.05 mmol substrate, CO_2 atmosphere, simulated light: 100 mW cm^{-2} , time = 24 h, and temperature = 25°C ; the yield of products was determined by GC and GC-MS analyses.



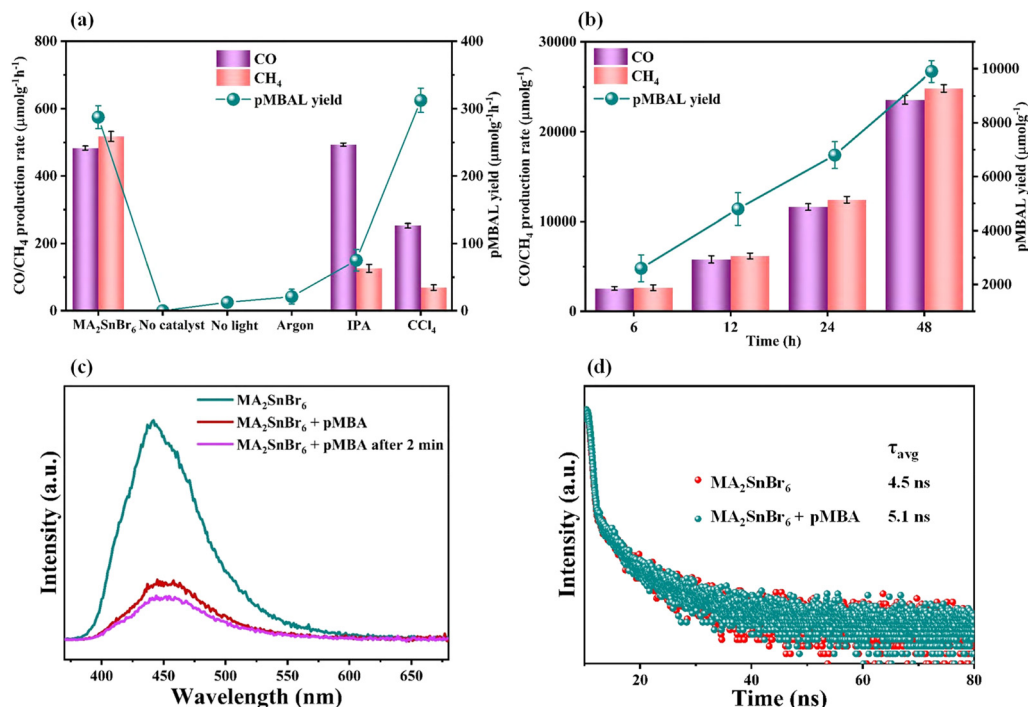


Fig. 3 (a) Photocatalytic reaction under different conditions, (b) time study, (c) PL spectra of MA₂SnBr₆ (PL excitation wavelength = 350 nm), and (d) time-resolved PL spectra of MA₂SnBr₆ (excitation wavelength 390 nm).

light of 400, 420, 450, and 500 nm and was compared with the DR UV-Vis absorption spectra of MA₂SnBr₆ (Fig. S9). Notably, the highest AQY of 2.75% was attained at 400 nm in comparison to 1.88%, 0.92%, and 0.19% at 420, 450, and 500 nm, respectively, demonstrating a conspicuous relation between the irradiated spectral profile and photocatalytic activity of MA₂SnBr₆. Moreover, applicability of MA₂SnBr₆ QDs was explored for the oxidation of lignin model compound and various biomass-derived alcohols (Table 1), with simultaneous CO₂ reduction to CO and CH₄ (entries 1–8). Interestingly, the alcoholic group in 2-phenoxy-1-phenyl-ethanol, a lignin model compound, was selectively oxidized to a keto group without affecting other moieties or the core structure of the substrate. In addition, vanillyl alcohol, veratryl alcohol, furfuryl alcohol, benzyl alcohol, *p*-chlorobenzyl alcohol, and *p*-methylbenzyl alcohol were oxidized to their corresponding aldehydes with synergistic CO₂ reduction to CO and CH₄ (entries 3–8).

Here, the synergistic CO₂ reduction with biomass-derived alcohol oxidation shows marked differences in product selectivity. These differences can be explained by considering the structural and electronic properties of alcohol substrates, such as resonance (*R*) and inductive (*I*) effects. *p*-Methoxybenzyl alcohol (entry 1) shows nearly equal production of CO and CH₄, attributed to the strong +*R* effect of the methoxy group, which increases the electron density on the benzylic carbon and promotes efficient oxidation, releasing sufficient electrons and protons for CO and CH₄ production. A similar trend is observed in the case of *p*-methylbenzyl alcohol (entry 8), where the +*I* and hyperconjugative effects of the methyl group promote CH₄ production. In contrast, significant CH₄ production occurred in the case of *p*-chlorobenzyl alcohol (entry 7) despite the –*I*

effect of the chloro group, possibly due to its moderate +*R* effect, which causes partial retention of electron density on the benzylic carbon. Further, benzyl alcohol (entry 6), where no substituent group is present, has higher CH₄ formation than CO, indicating favorable proton and electron availability without any significant steric or electronic effect. Substrates such as 2-phenoxy-1-phenyl ethanol (entry 2) and veratryl alcohol (entry 4) exhibit higher CO selectivity, probably due to steric hindrance from bulky substituents and electron delocalization across the aromatic system, which can slow down the rate of oxidation and limit proton release, restricting CO₂-to-CH₄ conversion. Next, vanillyl alcohol (entry 3) possesses –OH and –OCH₃ groups, which make the benzene ring electron-rich and stabilize the radical on the ring itself, diverting oxidation from benzylic position. Moreover, vanillyl alcohol undergoes intramolecular hydrogen bonding, which may hinder the substrate-catalyst interaction, thereby limiting oxidation and making fewer protons available for CH₄ production. Notably, in the case of furfuryl alcohol (entry 5), only CO was produced, consistent with the electron-deficient furan ring, exhibiting –*I* and weak +*R* effects, which result in poor oxidation efficiency and minimal proton generation. Further, aliphatic alcohols, which are difficult to oxidize, provided corresponding aldehydes and esters in reasonably lower yields (entries 1 and 2, Table S1). In addition, the oxidation of benzylamine resulted in *N*-benzylidenebenzylamine in quantitative yields (entry 3, Table S1).

Electro- and photo-chemical studies of MA₂SnBr₆ QDs

Next, the photoelectrochemical measurements were carried out to inquire the charge transfer dynamics. First, the transient



photocurrent response was conducted where MA_2SnBr_6 exhibited a swift response when intermittent light was irradiated at an interval of ~ 30 s for 10 cycles (Fig. S10a). This proclaims the effective generation and separation of a significant number of charge carriers upon light illumination, emphasizing the critical role of light in generating photo-excited carriers.⁸ Subsequently, the electrochemical impedance spectroscopy (EIS) was conducted, where the Nyquist plot of MA_2SnBr_6 fitted to the Randles circuit model (Fig. S10b). It was found that the charge transfer resistance was significantly dropped after shining the light over the MA_2SnBr_6 electrode as compared to the dark state. This highlights the effective separation of charge carriers, facilitating enhanced charge migration across the surface of MA_2SnBr_6 .⁴⁵ The linear sweep voltammetry (LSV) was conducted to evaluate the CO_2 reduction activity of MA_2SnBr_6 (Fig. S11). It was observed that the current density was increased when the light was irradiated showing the efficient charge separation and transfer over the surface of MA_2SnBr_6 . Thereafter, the electrolyte was purged with CO_2 , and afterwards, LSV was performed. The increment in cathodic current accounts for the facile charge transfer of electrons from MA_2SnBr_6 to CO_2 , suggesting a good structure–activity relationship consistent with the photocatalytic experiments.

Recycling and reusability of MA_2SnBr_6 QDs in the photocatalytic reaction

The chemical resilience of halide perovskites remains a challenge under photocatalytic reaction conditions. Notably, many previous studies have overlooked recyclability assessments post-photocatalysis. Therefore, the robustness of MA_2SnBr_6 was evaluated by employing it for five cycles of recyclability experiments (Fig. S12). The recyclability experiments revealed that the yields of pMBAL, CO, and CH_4 were maintained without any significant decrease in photocatalytic activity, showcasing the excellent reusability of the MA_2SnBr_6 photocatalyst. After completing five cycles, the photocatalyst was examined by PXRD (Fig. S13a), DRUV-Vis spectroscopy (Fig. S13b), XPS (Fig. S14a–d), TEM (Fig. S15a), and HRTEM (Fig. S15b). The results indicated no change in the crystal structure, optical properties, surface characteristics, and morphology of MA_2SnBr_6 , further proving its structural integrity even after repeated use.

Reaction mechanism of the MA_2SnBr_6 QDs promoting the photocatalytic reaction

To investigate the underlying mechanism of the photoredox reaction of MA_2SnBr_6 , illustrating the CO_2 reduction coupled with biomass-derived alcohol oxidation, controlled experiments were conducted. First, the model reaction was carried out under an argon atmosphere, where no CO and CH_4 were formed, showing that these products are exclusively formed through the photoreduction of supplied CO_2 rather than from the degradation of the catalyst, solvent, or substrate (Fig. 3a). Additionally, $21 \mu\text{mol g}^{-1} \text{h}^{-1}$ of pMBAL was produced under an Argon atmosphere owing to the photogenerated hole-assisted oxidation of pMBA. Further, the isotopic labeling study was performed by supplying $^{13}\text{CO}_2$ gas instead of $^{12}\text{CO}_2$ to track

the origin of formed CO and CH_4 (Fig. S16). After the photocatalytic reaction, the gaseous samples were injected into GC-MS (Fig. S17), which detected the signal for ^{13}CO and $^{13}\text{CH}_4$ with m/z 29 and m/z 17, respectively (Fig. S18a and b), authenticating that CO_2 is the only source to produce CO and CH_4 . Subsequently, a scavenger study was performed using CCl_4 as an electron scavenger, where the production rate of CO and CH_4 was significantly hampered, while the yield of pMBAL was comparatively increased. This result indicates that photogenerated electrons are responsible for CO_2 reduction (Fig. 3a). When IPA was employed as a hole scavenger, a slight increase in CO production was observed with a noticeable decrease in CH_4 yield compared to the optimized condition, whereas the pMBAL yield decreased significantly, which indicated the importance of holes in the oxidation of pMBA to pMBAL (Fig. 3a). The use of ethyl acetate as an aprotic solvent reduced the CH_4 production rate, as it cannot supply protons necessary for CH_4 formation, indicating that pMBA serves as the proton source in the reaction medium. The protons released during the oxidation of pMBA to pMBAL are essential for CH_4 generation. However, the introduction of IPA suppresses this oxidation by scavenging photogenerated holes, thereby reducing proton availability in the reaction mixture. Consequently, the decreased proton concentration ultimately limits the formation of CH_4 . The *in situ* electron paramagnetic resonance experiments were conducted to trap the $\text{C}\alpha$ radical of pMBA. The spin trap agent 5,5-dimethyl-1-pyrrolidine nitrogen oxide (DMPO) was used to trap the $\text{C}\alpha$ radical of pMBA, and the resulting spectra (Fig. S19) presented a signal of six characteristic peaks, validating the formation of the adduct DMPO- $\text{C}\alpha$ radical, verifying the intermediate α -hydroxy benzyl radical generation during photo-oxidation of pMBA to pMBAL.

Next, the photoluminescence (PL) study of MA_2SnBr_6 was carried out at an excitation wavelength (λ_{ex}) of 350 nm (Fig. 3c). A broad PL spectrum was observed, having a peak maximum of around 440 nm, which could be assigned to trap states. On subsequent addition of pMBA into MA_2SnBr_6 , the PL emission intensity significantly decreased, which infers the participation of charge carriers in the oxidation of pMBA. Fig. 3d shows the time-resolved PL (TRPL) decay profile of MA_2SnBr_6 , which reveals an average charge carrier lifetime of 4.5 ns. Upon the addition of the pMBA substrate, the decay dynamics significantly slowed down, resulting in an increased lifetime to 5.1 ns. The possible reason for this observation is the oxidation of pMBA, which is assisted by photogenerated holes, indicating that pMBA functions as an effective hole scavenger. The delayed dynamics suggest the active participation of photogenerated holes in the oxidation process, where they react with pMBA present in the system, facilitating its oxidation and leading to an increased average lifetime of charge carriers.

The excited-state dynamics of any catalyst significantly influences its photocatalytic activity.^{46,47} Hence, in order to delve deeper into the excited charge carrier dynamics of MA_2SnBr_6 , we performed ultrafast transient absorption (TA) studies after 400 nm pump excitation. Fig. 4a shows the TA spectra of bare MA_2SnBr_6 upon 400 nm pump excitation,



scanning in the spectral range from 420 nm to 650 nm at different pump–probe delay time scales. The pump fluence of $400 \mu\text{J cm}^{-2}$ was used at which the possibility of auger recombination is negligible (as discussed in SI). The TA spectrum of MA_2SnBr_6 exhibits a positive absorption band spanning across the entire visible region, which peaked at 450 nm. This positive signal can be attributed to the excited state's absorption (ESA) of trapped charge carriers.^{48,49} Earlier, O. M. Bakr and co-workers similarly observed a positive band in the visible region upon 380 nm excitation for other lead-free perovskites, CsMnBr_3 .⁵⁰ It is intriguing to see that no transient bleaching is observed here, which is possibly due to the presence of a large number of defects in MA_2SnBr_6 .⁴⁸ Keli Han and co-workers also observed a positive signal for the hydrothermally synthesized lead-free inorganic perovskite $(\text{Rb}_{0.75}\text{Cs}_{0.25})_3\text{InCl}_6$ and attributed this signal to photoinduced absorption from trap states.⁵¹

Further, we probed the TA kinetics of pristine MA_2SnBr_6 at a band maxima position of ~ 450 nm (Fig. 4b) to investigate the charge carrier dynamics. The rise time of the signal was found to be 0.3 ps (Table S2), which suggests that there is almost no potential barrier for the trapping of the charge carriers.⁵¹ Further, the recovery dynamics were fitted with a bi-exponential function, obtaining two decay components (Table S2): an ultrafast time-scale component τ_1 of 5.8 ps and a long lifetime component $\tau_2 > 1$ ns. Here, the fast recovery component ($\tau_2 = 5.8$ ps) can be assigned to the surface defect trapping or cooling of hot self-trapped excitons in MA_2SnBr_6 .⁴⁸ The long-timescale component ($\tau_2 > 1$ ns) is ascribed to the charge carrier recombination. Further, we conducted quenching

experiments with electron and hole quenchers to determine whether the transient signal originated due to trapped holes or electrons. Fig. 4b and c show the comparative kinetics of bare perovskites before and after adding electron and hole quenchers, respectively. The signal intensity decreased (Fig. S20) in the presence of the electron scavenger, and faster decay dynamics were observed (Fig. 4b). The first recovery component τ_1 decreased from 5.8 ps to 4.1 ps after adding the electron scavenger. Photogenerated electrons are scavenged by electron scavengers, leaving fewer electrons to recombine with the holes. Hence, the decrease in the transient signal intensity and faster recovery suggested that the signal corresponds to the trapped electrons. Thus, the transient signal in bare MA_2SnBr_6 can be easily assigned to ESA from trap states presented near the conduction band edge. However, in the presence of a hole-trapping agent, the decay dynamics became drastically slow (Fig. 4c), which validated the findings of the electron quenching experiment. The hole quencher scavenges the holes, leaving more electrons than holes. Hence, the slower decay observed further confirmed that electrons have a major contribution in the transient absorption signal of MA_2SnBr_6 .

Next, we performed *in situ* transient studies in the presence of CO_2 to examine its reactivity with photo-generated charge carriers in the bare MA_2SnBr_6 perovskite. Fig. 4d shows the comparative dynamics of bare MA_2SnBr_6 in the absence and presence of CO_2 . The decay dynamics becomes faster in the presence of CO_2 than in the bare MA_2SnBr_6 perovskite. The first recovery component τ_1 decreased from 5.8 ps in bare MA_2SnBr_6 to 4.9 ps in the presence of CO_2 . As explained earlier, the transient signal observed is due to the ESA of trapped electrons.

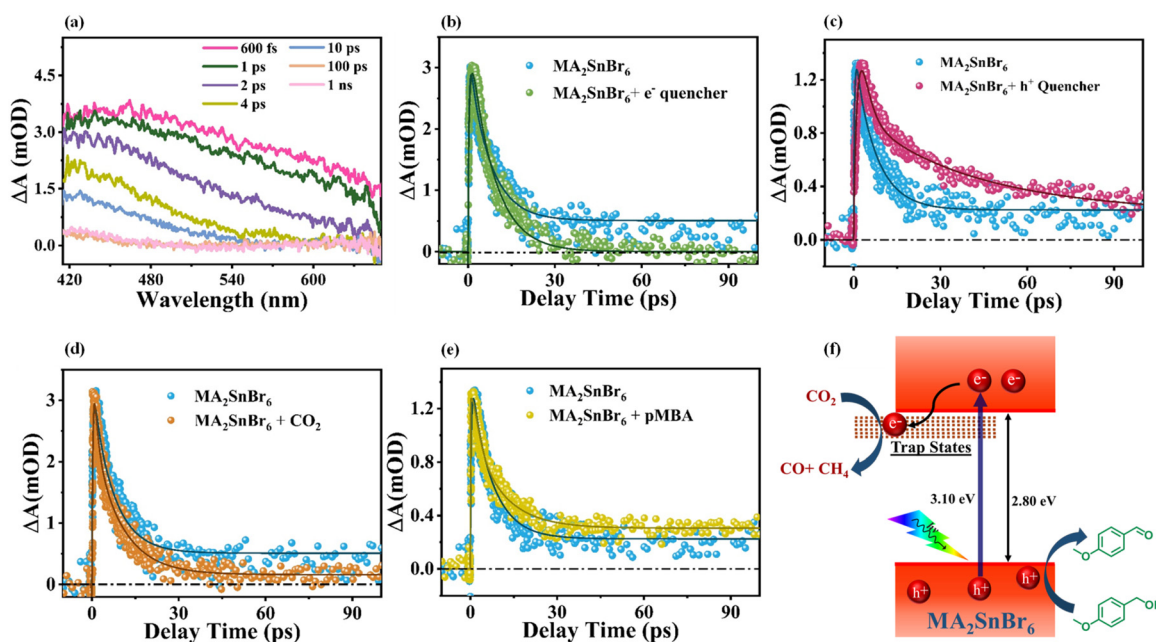


Fig. 4 (a) Transient absorption spectra of bare MA_2SnBr_6 , scanning range from 415 nm to 650 nm upon 400 nm pump excitation at various pump–probe delay time scales. Comparative dynamics between bare MA_2SnBr_6 and in the presence of (b) an electron scavenger, (c) hole scavenger, (d) CO_2 , and (e) pMBA upon 400 nm excitation. (f) Schematic of electron and hole pair generation in MA_2SnBr_6 QDs under 3.1 eV pump energy and their interaction with CO_2 and pMBA.



Hence, the faster decay dynamics confirmed the active participation of MA_2SnBr_6 electrons in the CO_2 reduction process,⁵² as schematically illustrated in Fig. 4f. In addition to that, we conducted ultrafast studies in the presence of pMBA to investigate the mechanism behind its oxidation. Fig. 4e represents the transient dynamics in the presence of pMBA. The slower dynamics was observed in the presence of alcohol substrates. The faster component (τ_1) increased from 5.8 ps to 8.8 ps in the presence of pMBA. This delay in recovery suggests that holes are reacting with pMBA present in the system, eventually helping in the formation of pMBAL. Fig. 4f illustrates the photo-physical mechanism responsible for the CO_2 reduction and pMBA oxidation. The 3.1 eV pump generates the electrons and holes within the conduction and valence bands, respectively. The conduction band electrons diffuse to trap states, which react with CO_2 molecules, producing CO and CH_4 . Conversely, the photogenerated holes react with biomass-derived pMBA to produce pMBAL.

The topographical image of MA_2SnBr_6 obtained *via* atomic force microscopy (AFM) is shown in Fig. S21, and its corresponding height profile reveals a thickness of 170 nm. Kelvin probe force microscopy (KPFM) was performed under dark and light conditions to analyze changes in the surface potential (Fig. 5a and c). In the dark, MA_2SnBr_6 delivers a contact

potential difference (CPD) of 350 mV, which increased to 391 mV under illumination (Fig. 5b and d). The surface potential voltage (SPV) is defined as the change in the surface potential in the dark and under light irradiation ($\text{SPV} = \text{CPD}_{\text{light}} - \text{CPD}_{\text{dark}}$), and is related to the photogenerated charge separation. The observed positive increment in CPD after irradiation of light ($\Delta\text{CPD} = 41$ mV) suggests a more significant accumulation of photogenerated holes over the MA_2SnBr_6 surface than in the dark, enhancing exciton separation and improving the photocatalytic activity.⁵³ To delve deeper into the mechanistic insights, the CO_2 temperature-programmed desorption (CO_2 -TPD) analysis was performed to observe the adsorption behavior of CO_2 over MA_2SnBr_6 (Fig. S22). The strong desorption peak observed between 180 and 190 °C indicates chemisorbed CO_2 molecules over the surface of MA_2SnBr_6 .

Computational studies

Further, CO_2 adsorption and activation on MA_2SnBr_6 were comprehensively studied by first-principles-based computational simulations, which elucidated the detailed mechanisms and pathways of the CO_2 reduction reaction (Fig. 6a). Following the experimental results, two primary CO_2 reduction pathways are considered: CO_2 to CO and CO_2 to CH_4 . Band-decomposed charge density analysis reveals that the localized charge around

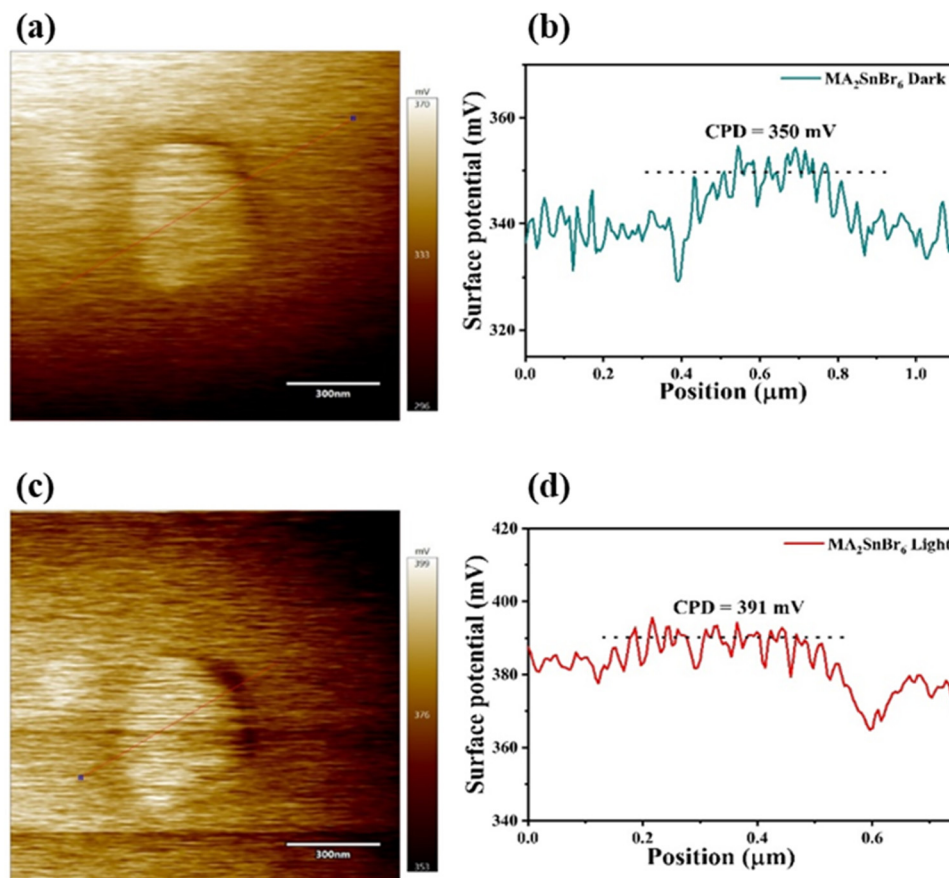


Fig. 5 KPFM images of MA_2SnBr_6 under (a) dark conditions and (b) its corresponding contact potential difference profile and (c) under light conditions and (d) its corresponding contact potential difference profile.



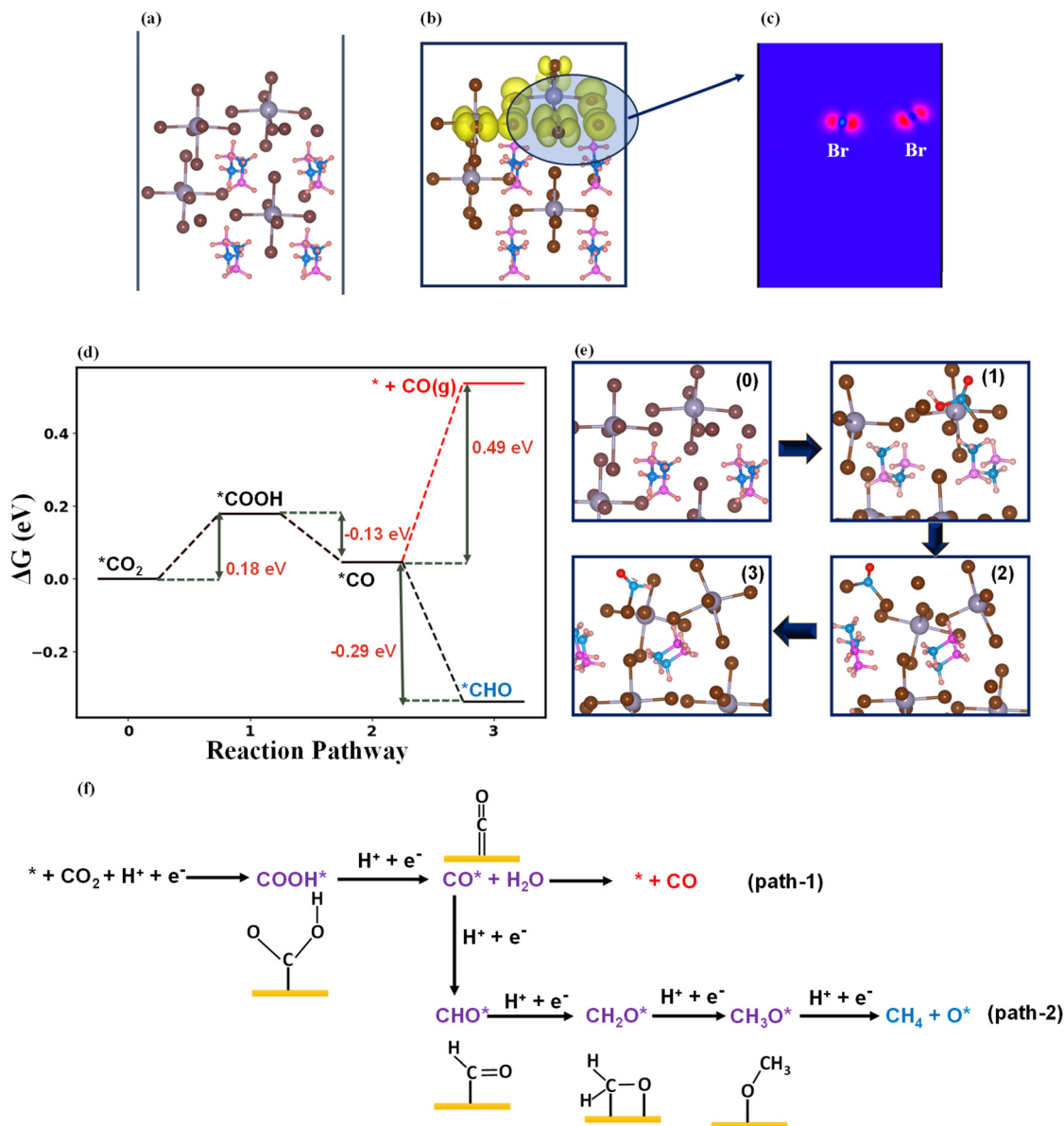


Fig. 6 (a) Optimized structure of MA₂SnBr₆. (b) Band decomposed charge density plot at the defect state. (c) 2D plot for localized charge density at the Br atom. (d) Reaction energy profile for CO₂-to-CO and CO₂-to-CH₄ reduction. (e) Optimized structures of the catalyst and various intermediates involved in the reaction pathway (the number in each box represents the step number assigned in the reaction energy profile). (f) Schematic showing the mechanism for CO₂ reduction over the surface of the MA₂SnBr₆ photocatalyst. Color keys: gray, tin; brown, bromine; blue, carbon; pink, nitrogen; and orange, hydrogen.

Br atoms originates from Br p-orbitals, indicating their critical role in CO₂ reduction reaction (Fig. 6b and c). The Br active sites, enriched at the surface, play a pivotal role in CO₂ activation and intermediate stabilization. As validated by XPS, a higher concentration of Br on the surface of MA₂SnBr₆ was observed (Fig. S2a), and computational results further highlight the localization of charge density around Br p-orbitals, making it a key catalytic site, thereby enhancing the catalytic efficiency of MA₂SnBr₆.

Density functional theory calculations were conducted to optimize the photocatalyst design by simulating the reaction energetics of the CO₂ reduction reaction, as shown in Fig. 6d.

The optimized structures of the catalyst MA₂SnBr₆ and various intermediates involved in the reaction pathway are displayed in Fig. 6e, and the plausible mechanism for CO₂ reduction on the MA₂SnBr₆ surface is presented in Fig. 6f. Typically, the photocatalytic CO₂ to CO or CH₄ reduction steps include the first proton-coupled electron transfer to generate a carboxyl intermediate (*COOH), and subsequently, the second charge transfer (one electron and one proton) for the formation of *CO intermediate as well as the desorption of CO for the final CO product (Fig. 6f, path-1). For CO₂ to CH₄, the reaction proceeds through path-2: CO₂ → COOH* → CO* → CHO* → CH₂O* → CH₃O* → CH₄. Note that the adsorption energy value is scaled



down to 0 eV here to track the energy changes in subsequent steps precisely. The formation of the COOH* intermediate is uphill by 0.18 eV. However, the transformation of COOH* to *CO is slightly downhill in energy by 0.13 eV. The formation of *COOH and its conversion to *CO are critical intermediates that determine the thermodynamics of the reaction pathway. At this stage, two competing possibilities arise: (1) desorption of CO as the final product or (2) the further reduction of *CO to form *CHO, leading to the formation of CH₄. DFT calculations reveal that the desorption of CO from the catalytic surface requires an energy input of 0.49 eV, making this step thermodynamically feasible under appropriate reaction conditions. However, the formation of the *CHO intermediate is energetically downhill by −0.38 eV, favoring the progression towards CH₄ formation. This downhill energy profile for *CHO formation indicates that, given sufficient energy, the catalyst can selectively drive the reduction pathway toward methane instead of terminating at carbon monoxide.

Despite the thermodynamic feasibility of both pathways, the rate-determining step (RDS) in the CO₂ reduction process is the desorption of CO, which requires an energy input of 0.49 eV. This RDS acts as a bottleneck for CO formation, potentially limiting the efficiency of the CO₂ reduction when CO is the desired product. However, the experimentally determined band gap of the photocatalyst is 2.8 eV, which is significantly higher than the energy required for CO desorption. Under light illumination, the catalyst generates sufficient photoexcitation energy to overcome the desorption barrier, ensuring that both CO desorption and subsequent *CHO formation become thermodynamically and kinetically favorable. This observation highlights the dual capability of the photocatalyst to selectively produce either CO or CH₄, depending on the operating conditions.⁵⁴ The computational analysis and comparison with experimental findings confirm that the photocatalyst can facilitate both CO and CH₄ production.

These insights underscore the importance of catalyst design in tuning the product selectivity for the photocatalytic CO₂ reduction reaction. The detailed mechanistic study highlights the dual functionality of the MA₂SnBr₆ surface in facilitating both CO₂-to-CO and CO₂-to-CH₄ conversions. The localized charge density on Br *p*-orbitals enhances the catalytic efficiency, and the system's band gap provides sufficient driving force for CO₂-to-CO and CO₂-to-CH₄ conversion. These findings underline the potential of MA₂SnBr₆ as an efficient photocatalyst for CO₂ reduction.

Furthermore, the photocatalytic activity of MA₂SnBr₆ for CO₂ reduction was compared with previously reported perovskites, as shown in Fig. 7 and Table S3. It was observed that most of the prior studies utilized lead-based perovskites, predominantly complex perovskite heterojunctions, and yet suffered a low production rate of CO. Moreover, even after significant attempts, the photoreduction of CO₂ to CH₄ was still not promising as it is an 8 e[−] process and demands high energy as compared to the 2 e[−] reduction process of CO₂ to CO. Therefore, addressing the challenge, MA₂SnBr₆ displayed a remarkable electron consumption rate (*R_e*) of 5110 μmol g^{−1} h^{−1} under simulated light and 12383 μmol g^{−1} h^{−1} under natural sunlight, significantly surpassing previously reported halide perovskite-based systems.

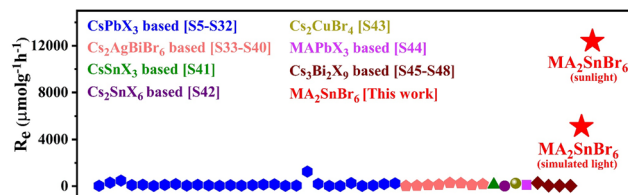


Fig. 7 Comparison of the electron consumption rate (*R_e*) of previously reported halide perovskites. The referenced articles: ref. [S1–S44].

Consequently, as a lead-free, single-component material, MA₂SnBr₆ not only achieves a superior CO₂ reduction rate with a higher production rate of CO and CH₄ but also simultaneously facilitates the photo-oxidation of biomass-derived compounds into value-added chemicals.

Conclusions

We successfully addressed the synergistic transformation of CO₂ and biomass valorization to solar fuels and high-value fine chemicals utilizing the hybrid halide perovskite MA₂SnBr₆. Herein, the stability, reusability, toxicity, and efficiency issues of hybrid halide perovskites (HHPs) were solved. The air-stable, ambient, and polar solvent-friendly vacancy-ordered MA₂SnBr₆ QDs are disguised in solving one of the major challenges while dealing with the halide perovskites. For the first time, MA₂SnBr₆ QDs were employed in a photoredox process for CO₂ reduction, and the icing on the cake is the simultaneous oxidation of biomass-derived alcohols to value-added products. MA₂SnBr₆ displayed an exceptionally high electron consumption rate (*R_e*) of 5110 μmol g^{−1} h^{−1} under simulated light and 12383 μmol g^{−1} h^{−1} under natural sunlight, significantly surpassing previously reported halide perovskite-based systems. Based on *in situ* transient absorption, *in situ* EPR experiments, and computational studies, the detailed mechanism is unravelled for this photo-redox reaction to valorise CO₂ and biomass-based feedstocks. Consequently, as a lead-free, single-component material, without any co-catalyst and sacrificial agent, MA₂SnBr₆ not only achieves significantly higher yields of CO and CH₄ but also synergistically facilitates the photo-oxidation of biomass-derived alcohols into valuable chemicals, making a significant contribution towards sustainable solar fuel generation and fine chemical production.

Experimental section

Chemicals

Methylamine hydrobromide, ethyl acetate, and tetrabutylammonium hexafluorophosphate were purchased from TCI Chemicals, India. Isopropanol, acetonitrile, and tin(IV) bromide were purchased from Sigma-Aldrich, India. Ethanol was purchased from Merck, India.

Characterization

A Bruker D8 Advanced diffractometer, which featured a scintillation counter detector and operated with Cu-Kα radiation



($\lambda = 0.15418$ nm, $2\theta = 5\text{--}80^\circ$, scan rate = 4° min^{-1}) source at 40 kV and 40 mA, was used to obtain powder X-ray diffraction (PXRD) patterns. The Raman spectrum was recorded using a WI Tech Raman Spectrometer with a 632 nm He-Ne laser. Diffuse reflectance spectra were recorded using an Agilent Cary 100 UV-vis spectrophotometer. ATR-FTIR spectroscopy was performed using a Bruker Vertex 70 spectrometer. X-ray photoelectron spectroscopy (XPS) and ultraviolet photoelectron spectroscopy (UPS) measurement of MA_2SnBr_6 was performed using an Al K α X-ray source and a monochromator with ultra-high vacuum provided by Thermo Fisher Scientific. The He(I) (21.22 eV) gas discharge lamp was used as a source during UPS measurements. A Bruker Avance NEO 400 was employed for the measurement of solid-state MAS NMR spectra of ^{119}Sn , ^{79}Br , ^{13}C , and ^{15}N using a 5 mm FG NMR probe. Solid-state photoluminescence spectra (PL) were recorded using a Horiba Fluorolog instrument, and PL decay was studied using a TCSPC (time-correlated single-photon counting) assembly of the Horiba Fluorolog instrument. The SEM (scanning electron microscopy) images were collected using a JEOL instrument (JSM-7610FPlus). The morphology of MA_2SnBr_6 and the particle size of MA_2SnBr_6 were analyzed using a transmission electron microscope (TEM, JEOL) and a high-resolution TEM (HRTEM) at an accelerating voltage of 120 kV. EPR analysis was performed using a Bruker A300-9.5/12/S/W system. The measurement was performed at 25°C using UV-Vis light procured from LOT-Quantum Design. For the experiment, 2 mg of MA_2SnBr_6 was dispersed in 1 mL of ethyl acetate followed by the addition of 10 μL of pMBA and spin-trap agent DMPO. The reaction mixture was purged with Ar to ensure an inert atmosphere. Initially, the EPR spectrum was recorded in the dark. Subsequently, the sample was illuminated for 30 min and the spectrum was recorded. The data acquisition setting involved a centre field of 3500 G, a sweep width of 300 G, and a static field of 3450 G with a modulation frequency of 100 kHz, a modulation amplitude of 4.91 G, and a sweep time of 81.92 s. The atomic force microscopy (AFM) and Kelvin probe force microscopy (KPFM) were performed using an Asylum Research MFP-3D AFM model with a Ti/Ir tip in the tapping mode. A Shimadzu GC-2014 instrument equipped with a mass detector was used to analyze the reaction products.

Electrochemical measurement

Electrochemical analysis was performed in a standard three-electrode cell (a platinum wire as the counter electrode, a Ag/AgCl electrode as the reference electrode, and 0.1 M tetrabutyl ammonium hexafluorophosphate in dichloromethane as the electrolyte solution) using a Metrohm Autolab workstation. The ITO electrode coated with a catalyst was used as the working electrode and a 400 W xenon lamp was used as the light source. Prior to the use of the ITO substrate, it was washed by sonication in H_2O , isopropanol, acetone, and again in H_2O , and then the substrate was kept for drying in the oven. Then, 5 mg of MA_2SnBr_6 catalyst was dispersed in 50 μL of ethanol with 5 μL of Nafion. The prepared dispersion (10 μL) was drop-cast over the 0.25 cm^2 area of the ITO electrode and allowed to dry at room temperature. The estimated amount of catalyst loading over the ITO electrode was about 0.8 mg cm^{-2} . All the

electrochemical measurements were carried out at 25°C . Linear sweep voltammetry (LSV) run was carried out at 10 mV s^{-1} scan rate, and the potential value was reported in V vs. Ag/AgCl. CO_2 was purged into the system for 30 min and LSV was recorded for the CO_2 -saturated electrolyte. To record the electrochemical impedance spectroscopy (EIS) spectra, a potential amplitude of 10 mV in the frequency range of 0.01 Hz to 100 kHz was employed. The Nova 2.1 FRA software was employed to analyse the impedance spectra.

Transient absorption spectroscopy

Transient absorption spectroscopy was performed using a Ti:sapphire laser system with the regenerative 800 nm output pulsed at 1 kHz. The output was divided into two paths by a 70–30 beam splitter. The 30% of output of the regenerative pulse passed through the delay generator with a temporal resolution of 10 fs and focused on a sapphire crystal to produce a continuum probe pulse covering from 420 to 750 nm. The 70% percent of the output entered the spectrometer, where it passed through a BBO crystal to generate a 400 nm pump pulse. The pump pulse was chopped at 500 Hz and focused perpendicular to the sample. The acquired data were analysed using Surface Explorer software. First, scattered light was subtracted from each scan prior to chirp correction. Later on, transient spectra were taken at specific time delay, and the kinetics was fitted at a particular probe wavelength. The samples were kept under continuous stirring to avoid the degradation of the sample. AgNO_3 and KI were used as electron and hole scavengers, respectively, for transient studies.

Computational details

The DFT calculations are performed using the Vienna Ab initio Simulation Package (VASP)⁵⁵ with frozen-core projector augmented wave (PAW) pseudopotentials.⁵⁶ The Perdew–Burke–Ernzerhof (PBE) functional of the generalized gradient approximation (GGA) was employed for the exchange–correlation potential. Long-range van der Waals (vdW) interactions were calculated using the empirical correction method PBE + D3.⁵⁷ A Γ -centered Monkhorst–Pack mesh with k -points of $1 \times 3 \times 3$ was used for the simulations, and the plane wave energy cutoff was set to 420 eV.⁵⁸ The convergence criterion for electronic optimization was 10^{-6} eV, while atomic optimizations were deemed complete when the forces on atoms were below 0.02 eV \AA^{-1} . To simulate the MA_2SnBr_6 system, a vacuum of 40 \AA was introduced along one direction. A surface was created, and the top layers are relaxed during optimization, while the remaining layers were fixed in their bulk geometry. The Fermi level was set to zero for the band structure and density of states (DOS) calculations, and Gaussian smearing was applied with a width of 0.02 eV. The VASPKIT tool was used for post-processing, including the calculation of Gibbs free energy.

The adsorption-free energy (ΔG^*) and adsorption energies of reactants and intermediates were calculated using the following equation:

$$\Delta G = \Delta E + \Delta E_{\text{ZPE}} - T\Delta S$$

$$\Delta E_{\text{abs}} = E_{\text{slab/(molecule)}} - (E_{\text{slab}} + E_{\text{molecule}})$$



where * represents the active site of the catalyst. The zero-point energy (ZPE) term, ΔE_{ZPE} , is derived from computed vibrational frequencies. The terms $E_{\text{slab/(molecule)}}$, E_{slab} , and E_{molecule} represent the total energies of the slab with adsorbed intermediates/molecules, the bare slab, and the isolated molecule, respectively.

Synthesis procedure

Vacancy-ordered methyl ammonium tin bromide (MA_2SnBr_6) perovskite QDs were synthesized for the first time *via* a straightforward mechanochemical route, where MABr (methylammonium bromide) and SnBr_4 (tin(IV) bromide) were taken in 1 : 1 stoichiometric ratio as a starting material and ground in a mortar and pestle. A yellow powder was obtained *via* this solvent-free and eco-friendly process. The MA_2SnBr_6 powder was then recrystallized in ethanol to produce MA_2SnBr_6 crystals.

Photocatalytic experiment

The photocatalytic activity of MA_2SnBr_6 was tested under a solar simulator (Oriel AM 1.5 at 100 mW cm^{-2} intensity). In a typical reaction, 5 mL of ethyl acetate and 0.05 mmol of *p*-methoxybenzaldehyde were taken in a round-bottom flask containing a certain amount of catalyst. The reaction mixture was sonicated and purged with argon for 10 min. The reaction mixture was purged with a balloon filled with CO_2 for 30 min and then the round-bottom flask was sealed. After the reaction, the gaseous sample was injected into a Shimadzu gas chromatograph (2014) equipped with an FID detector. After that, the liquid mixture was separated by centrifugation and filtration for quantitative and qualitative analyses. The liquid products were analyzed using a Shimadzu gas chromatograph-mass spectrometer (GC-MS).

Author contributions

Bhawna Rawat: conceptualization, methodology, investigation, writing – original draft, data curation, and visualization; Ankita Kumari: computational studies, writing; Manvi Sachdeva: performed transient absorption experiments and writing; Himanshu Bhatt: transient absorption methodology, data analysis; Dibyajyoti Ghosh: computational studies, writing – review and editing; Hirendra N. Ghosh: writing – review and editing; Rajenahally V. Jagadeesh: writing – review and editing; Kamalakannan Kailasam: conceptualization, supervision, writing – review and editing, project administration, funding acquisition.

Conflicts of interest

There are no conflicts to declare.

Data availability

The data supporting this article have been included as part of the SI. See DOI: <https://doi.org/10.1039/d5cy00169b>.

Acknowledgements

B. Rawat thanks UGC New Delhi for fellowship under Grant 191620176340/(CSIR UGC NET) and INST Mohali for instrumental facilities. Prof. K. Kailasam expresses thanks to Anusandhan National Research Foundation (ANRF) for the Core Research Grant (CRG), sanction order No. CRG/2023/001875. Rajenahally V. Jagadeesh thanks the support from the European Union under the REFRESH-Research Excellence for Region Sustainability and High-tech Industries project number CZ.10.03.01/00/22_003/0000048 *via* the Operational Programme Just Transition.

References

- 1 S. Yoshino, T. Takayama, Y. Yamaguchi, A. Iwase and A. Kudo, *Acc. Chem. Res.*, 2022, **55**, 966–977.
- 2 S. M. Han, M. Park, S. Kim, C. Jeong, J. Kim and D. Lee, *EES Catal.*, 2025, **3**, 723–732.
- 3 Y. Li, H. Liu, J. Raj, M. Pishnamazi and J. Wu, *EES Catal.*, 2025, **3**, 843–855.
- 4 A. Jaryal, A. K. Singh, S. Dhingra, H. Bhatt, M. Sachdeva, H. N. Ghosh, A. Indra and K. Kailasam, *EES Catal.*, 2024, **2**, 1019–1026.
- 5 H. Li, D. Regalado, C.-S. J. Wu, M. Prato, A. Treglia, H. Wang, W. Hempel, M. Sessolo, Y. Zhou, A. Olivati and A. Petrozza, *Energy Environ. Sci.*, 2025, **18**, 6618–6627.
- 6 W. Zhang, G. E. Eperon and H. J. Snaith, *Nat. Energy*, 2016, **1**, 16048.
- 7 J. Sheng, Y. He, J. Li, C. Yuan, H. Huang, S. Wang, Y. Sun, Z. Wang and F. Dong, *ACS Nano*, 2020, **14**, 13103–13114.
- 8 N. Li, X. Chen, J. Wang, X. Liang, L. Ma, X. Jing, D. L. Chen and Z. Li, *ACS Nano*, 2022, **16**, 3332–3340.
- 9 S. Li, H. Lin, C. Chu, C. Martin, W. MacSwain, R. W. Meulenberg, J. M. Franck, A. Chakraborty and W. Zheng, *ACS Nano*, 2023, **17**, 22467–22477.
- 10 H. Huang, H. Yuan, K. P. F. Janssen, G. Solís-Fernández, Y. Wang, C. Y. X. Tan, D. Jonckheere, E. Debroye, J. Long, J. Hendrix, J. Hofkens, J. A. Steele and M. B. J. Roeflaers, *ACS Energy Lett.*, 2018, **3**, 755–759.
- 11 J. Lee, S. P. Chai and L. L. Tan, *ACS Energy Lett.*, 2024, **9**, 1932–1975.
- 12 Z. Zhang, M. Shu, Y. Jiang and J. Xu, *Chem. Eng. J.*, 2021, **414**, 128889.
- 13 Y. F. Xu, M. Z. Yang, H. Y. Chen, J. F. Liao, X. D. Wang and D. Bin Kuang, *ACS Appl. Energy Mater.*, 2018, **1**, 5083–5089.
- 14 M. Shu, Z. Zhang, Z. Dong and J. Xu, *Carbon*, 2021, **182**, 454–462.
- 15 N. Li, J. Wang, G. Zhao, J. Du, Y. Li, Y. Bai, Z. Li and Y. Xiong, *ACS Mater. Lett.*, 2024, **6**, 999–1006.
- 16 A. Pan, X. Ma, S. Huang, Y. Wu, M. Jia, Y. Shi, Y. Liu, P. Wangyang, L. He and Y. Liu, *J. Phys. Chem. Lett.*, 2019, **10**, 6590–6597.
- 17 M. Ou, W. Tu, S. Yin, W. Xing, S. Wu, H. Wang, S. Wan, Q. Zhong and R. Xu, *Angew. Chem.*, 2018, **130**, 13758–13762.



- 18 Z. Mo, X. Zhu, Z. Jiang, Y. Song, D. Liu and H. Li, *Appl. Catal., B*, 2019, **256**, 117854.
- 19 J. F. Liao, Y. T. Cai, J. Y. Li, Y. Jiang, X. D. Wang, H. Y. Chen and D. Bin Kuang, *J. Energy Chem.*, 2020, **53**, 309–315.
- 20 L. Li, Z. Zhang, C. Ding and J. Xu, *Chem. Eng. J.*, 2021, **419**, 129543.
- 21 Z. C. Kong, H. H. Zhang, J. F. Liao, Y. J. Dong, Y. Jiang, H. Y. Chen and D. Bin Kuang, *Sol. RRL*, 2020, **4**, 1–7.
- 22 Z. C. Kong, J. F. Liao, Y. J. Dong, Y. F. Xu, H. Y. Chen, D. Bin Kuang and C. Y. Su, *ACS Energy Lett.*, 2018, **3**, 2656–2662.
- 23 Y. Jiang, J. F. Liao, Y. F. Xu, H. Y. Chen, X. D. Wang and D. Bin Kuang, *J. Mater. Chem. A*, 2019, **7**, 13762–13769.
- 24 Y. F. Xu, M. Z. Yang, B. X. Chen, X. D. Wang, H. Y. Chen, D. Bin Kuang and C. Y. Su, *J. Am. Chem. Soc.*, 2017, **139**, 5660–5663.
- 25 Y. Jiang, J. F. Liao, H. Y. Chen, H. H. Zhang, J. Y. Li, X. D. Wang and D. Bin Kuang, *Chem*, 2020, **6**, 766–780.
- 26 Y. Jiang, H. Y. Chen, J. Y. Li, J. F. Liao, H. H. Zhang, X. D. Wang and D. Bin Kuang, *Adv. Funct. Mater.*, 2020, **30**, 2–9.
- 27 J. Hou, S. Cao, Y. Wu, Z. Gao, F. Liang, Y. Sun, Z. Lin and L. Sun, *Chem. – Eur. J.*, 2017, **23**, 9481–9485.
- 28 Z. Chen, Y. Hu, J. Wang, Q. Shen, Y. Zhang, C. Ding, Y. Bai, G. Jiang, Z. Li and N. Gaponik, *Chem. Mater.*, 2020, **32**, 1517–1525.
- 29 S. Bera, A. Patra, S. Shyamal, D. Nasipuri and N. Pradhan, *ACS Energy Lett.*, 2022, **7**, 3015–3023.
- 30 Y. F. Xu, X. D. Wang, J. F. Liao, B. X. Chen, H. Y. Chen and D. Bin Kuang, *Adv. Mater. Interfaces*, 2018, **5**, 1–8.
- 31 F. Xu, K. Meng, B. Cheng, S. Wang, J. Xu and J. Yu, *Nat. Commun.*, 2020, **11**, 1–9.
- 32 L. Y. Wu, Y. F. Mu, X. X. Guo, W. Zhang, Z. M. Zhang, M. Zhang and T. B. Lu, *Angew. Chem., Int. Ed.*, 2019, **58**, 9491–9495.
- 33 X. Wang, J. He, L. Mao, X. Cai, C. Sun and M. Zhu, *Chem. Eng. J.*, 2021, **416**, 2–10.
- 34 X. Wang, J. He, J. Li, G. Lu, F. Dong, T. Majima and M. Zhu, *Appl. Catal., B*, 2020, **277**, 119230.
- 35 J. Wang, J. Wang, N. Li, X. Du, J. Ma, C. He and Z. Li, *ACS Appl. Mater. Interfaces*, 2020, **12**, 31477–31485.
- 36 S. Wan, M. Ou, Q. Zhong and X. Wang, *Chem. Eng. J.*, 2019, **358**, 1287–1295.
- 37 S. Kumar, I. Hassan, M. Regue, S. Gonzalez-Carrero, E. Rattner, M. A. Isaacs and S. Eslava, *J. Mater. Chem. A*, 2021, **9**, 12179–12187.
- 38 Z. Zhang, D. Li, Y. Chu, L. Chang and J. Xu, *J. Phys. Chem. Lett.*, 2023, **14**, 5249–5259.
- 39 Z. Zhang, Y. Jiang, Z. Dong, Y. Chu and J. Xu, *Inorg. Chem.*, 2022, **61**, 16028–16037.
- 40 X. D. Wang, Y. H. Huang, J. F. Liao, Y. Jiang, L. Zhou, X. Y. Zhang, H. Y. Chen and D. Bin Kuang, *J. Am. Chem. Soc.*, 2019, **141**, 13434–13441.
- 41 Q. M. Sun, J. J. Xu, F. F. Tao, W. Ye, C. Zhou, J. H. He and J. M. Lu, *Angew. Chem., Int. Ed.*, 2022, **61**, e202200872.
- 42 Y. Jiang, R. Zhou, Z. Zhang, Z. Dong and J. Xu, *J. Mater. Chem. C*, 2023, **11**, 2540–2551.
- 43 Z. Zhang, D. Li, Z. Dong, Y. Jiang, X. Li, Y. Chu and J. Xu, *Sol. RRL*, 2023, **7**, 1–10.
- 44 B. Rawat, V. R. Battula, P. K. Nayak, D. Ghosh and K. Kailasam, *ACS Appl. Mater. Interfaces*, 2023, **15**, 53604–53613.
- 45 B. Rawat, V. R. Battula, A. Kumari, D. Ghosh and K. Kailasam, *ACS Sustainable Chem. Eng.*, 2024, **12**, 13124–13136.
- 46 A. M. El-Zohry, B. Turedi, A. Alsalloum, P. Maity, O. M. Bakr, B. S. Ooi and O. F. Mohammed, *Commun. Chem.*, 2022, **5**, 1–7.
- 47 N. K. Tailor, S. Singh, S. K. Saini, Kaivalya, M. A. Afroz, M. Kumar, S. C. Peter, K. K. Pant and S. Satapathi, *Adv. Funct. Mater.*, 2024, **2402894**, 2–10.
- 48 D. Sebastian, A. Pallikkara, H. Bhatt, H. N. Ghosh and K. Ramakrishnan, *J. Phys. Chem. C*, 2022, **126**, 11182–11192.
- 49 P. Singh, G. Kaur, N. Ghorai, T. Goswami, A. Thakur and H. N. Ghosh, *Phys. Rev. Appl.*, 2020, **14**, 14087.
- 50 J. Almutlaq, W. J. Mir, L. Gutiérrez-Arzaluz, J. Yin, S. Vasylevskyi, P. Maity, J. Liu, R. Naphade, O. F. Mohammed and O. M. Bakr, *ACS Mater. Lett.*, 2021, **3**, 290–297.
- 51 P. Han, W. Zhou, D. Zheng, X. Zhang, C. Li, Q. Kong, S. Yang, R. Lu and K. Han, *Adv. Opt. Mater.*, 2022, **10**, 2101344.
- 52 X. Deng, J. Zhang, K. Qi, G. Liang, F. Xu and J. Yu, *Nat. Commun.*, 2024, **15**, 1–12.
- 53 R. Chen, S. Pang, H. An, J. Zhu, S. Ye, Y. Gao, F. Fan and C. Li, *Nat. Energy*, 2018, **3**, 655–663.
- 54 Y. Jing and T. Heine, *J. Mater. Chem. A*, 2018, **6**, 23495–23501.
- 55 G. Kresse and J. Furthmüller, *Phys. Rev. B: Condens. Matter Mater. Phys.*, 1996, **54**, 11169–11186.
- 56 G. Kresse and D. Joubert, *Phys. Rev. B: Condens. Matter Mater. Phys.*, 1999, **59**, 1758–1775.
- 57 S. Grimme, J. Antony, S. Ehrlich and H. Krieg, *J. Chem. Phys.*, 2010, **132**, 154104.
- 58 H. J. Monkhorst and J. D. Pack, *Phys. Rev. B*, 1976, **13**, 5188–5192.

